Differential interference contrast microscopy

Chapter · November 2012

Michael Shribak
Marine Biological Laboratory

M.Shribak, “Differential interference contrast (DIC) microscopy”. In: Biomedical Optical Phase Microscopy and Nanoscopy (eds. N. T. Shaked, Z. Zalevsky and L. L. Satterwhite), Elsevier, (2012).

CHAPTER 2

Differential Interference Microscopy

Michael Shribak
Marine Biological Laboratory, Woods Hole, MA

Editor: Lisa L. Satterwhite

2.1 Introduction

Differential interference contrast (DIC) light microscopy is widely used to observe structure and motion in unstained living cells and isolated organelles. DIC microscopy is a beam-shearing interference system in which the reference beam is sheared by a small amount, generally less than the diameter of an Airy disk. The technique produces a monochromatic shadow-cast image that displays the gradient of optical paths. Those regions of the specimen where the optical paths increase along a reference direction appear brighter (or darker), while regions where the path differences decrease appear in reverse contrast. As the gradient of optical path grows steeper, image contrast is significantly increased. Another important feature of the DIC technique is that it produces effective optical sectioning. This is particularly obvious when high numerical aperture (NA) objectives are used together with high NA condenser illumination.

The DIC technique was invented by Smith in 1947 [1,2]. He placed one Wollaston prism between a pair of polarizers at the front focal plane of the condenser and another Wollaston prism in the back focal plane of objective lens (Figure 2.1). The first Wollaston prism splits the input beam angularly into two orthogonally polarized beams. The condenser makes the beam axes parallel with a small shear. Then the objective lens joins them in the back focal plane where the second Wollaston prism introduces an angular deviation into the beam and makes them parallel. The splitting angles ε_1 and ε_2 are connected with the focal distances of the condenser and objective f_c and f_{ob} and the shear amount d by the following relation:

$$f_c\varepsilon_1 = f_{ob}\varepsilon_2 = d \tag{2.1}$$

This optical configuration creates a polarizing-shearing interferometer, by which one visualizes phase nonuniformity of the specimen. Smith originally called this device the

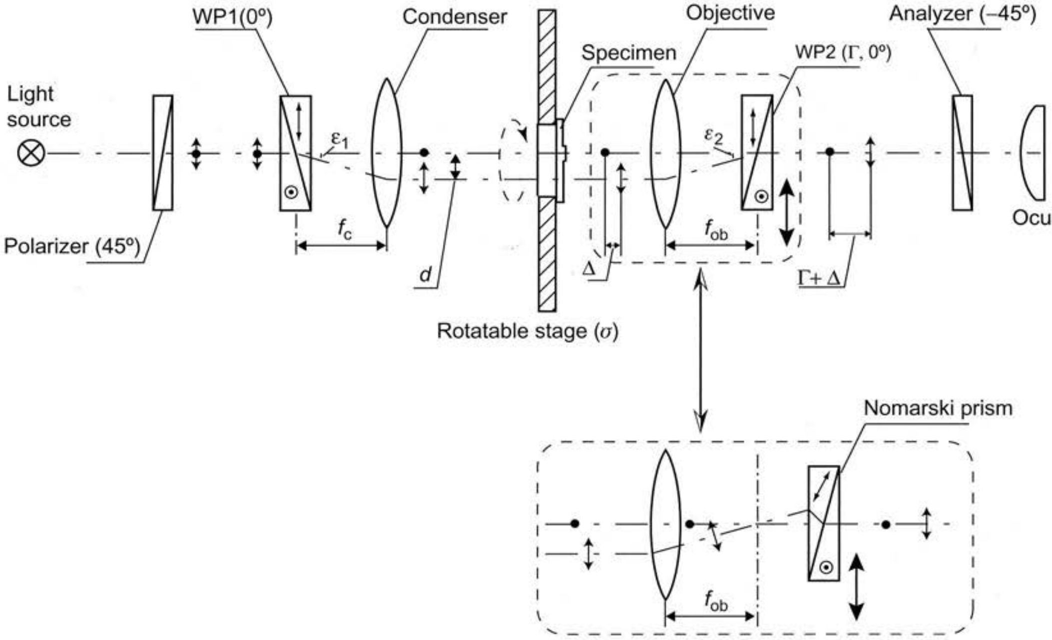

Figure 2.1

DIC microscope setup. Polarizer at 45° azimuth; WP1: first Wollaston prism at 0° azimuth; ε_1: splitting angle; f_c: condenser lens focal distance; d: shear amount; Δ: optical path difference introduced by specimen under investigation; σ: azimuth of rotatable stage; f_{ob}: objective lens focal distance; WP2: second Wollaston prism at 0° azimuth (the second prism introduces bias Γ); ε_2: splitting angle; analyzer at $-45°$ azimuth; Wollaston prism can be replaced by Nomarski prism.

"Smith double-refracting interference shearing microscope system." However, he also gave credit [2] to Lebedeff [3], who constructed the first double-refracting interference shearing microscope.

In addition, Smith [1,2] proposed another DIC microscope with the vertical shear direction, which he called the "Smith double-focus system." The system employed lenses made from birefringent crystals associated with the condenser and objective of the microscope, to impart a double-focus effect on two beams generated by the birefringence. The two lenses must be in conjugate positions, preferably at the front focal plane of the condenser and the back focal plane of the objective, respectively. However, Smith's double-focus DIC system did not find wide use.

The both Smith's approaches suffered from the same problem. In conventional medium to high numerical aperture (NA) objective lenses, the back focal plane is located inside the lens system and therefore not available for insertion of a Wollaston prism or a birefringent lens. In particular, in the shearing DIC microscope system, if the Wollaston prism is placed far from the back focal plane, the prism only makes the rays parallel. But those beams are spatially displaced and hence are not recombined. Therefore, the Smith-shearing DIC scheme requires special design for the microscope objective lenses so that the Wollaston prism can be incorporated within.

Nomarski [4,5] took another approach and proposed in 1952 the use of a special polarization prism. This Nomarski prism (see insert in Figure 2.1) introduced spatial displacement and angular deviation of orthogonally polarized beams simultaneously. The prism can therefore be placed outside of the objective lens. By using crystal wedges with appropriately oriented axes, the Nomarski prism recombines the two beams that were separated by the condenser Wollaston as though a regular Wollaston prism were located at the back aperture plane in the objective lens. This feature enables the use of the Nomarski DIC scheme with regular high NA microscope objectives.

A DIC image can be modeled as the superposition of one image over an identical copy that is displaced by a small amount d and phase shifted by bias Γ. For simplicity, consider a phase nonbirefringent specimen, which is described by Cartesian coordinates XOY in the object plane. The specimen is illuminated by monochromatic light with wavelength λ. The intensity distribution $I(x,y)$ in the images depends on specimen orientation and varies proportionally with the cosine of the angle made by the gradients azimuth θ and the relative direction of wavefront shear σ [6]:

$$I(x,y) = \tilde{I}\sin^2\left(\frac{\pi}{\lambda}(\Gamma + d\gamma(x,y)\cos(\theta(x,y)-\sigma))\right) + I_c(x,y) \tag{2.2}$$

where $\tilde{I}$ is the initial beam intensity, $\gamma(x,y)$ and $\theta(x,y)$ are the gradient magnitude and azimuth, and $I_c(x,y)$ corresponds to a constant offset of the intensity signal.

It follows from formula (2.2) that if the shear direction is parallel to the optical path gradient ($\theta - \sigma = 0^\circ$ or $\theta - \sigma = 180^\circ$) the image contrast is maximal. Where the shear direction is perpendicular to the gradients ($\theta - \sigma = 90^\circ$ or $\theta - \sigma = 270^\circ$) the contrast equals zero. Thus, the regular DIC technique shows the two-dimensional distribution of optical path gradients encountered along the shear direction. It is therefore prudent to examine unknown objects at several azimuth orientations [5,7].

The DIC microscopy demonstrates remarkable optical sectioning capability, like confocal microscopy. The depth in specimen space that appears to be in focus within the image, without readjustment of the microscope focus, is the depth of field. In a regular bright-field microscope, the total depth of field d_{tot} is given by the sum of the diffraction-limited wave and geometrical optical depths of field as [8,9]:

$$d_{\mathrm{tot}} = \frac{\lambda n}{\mathrm{NA}^2} + \frac{n}{M \times \mathrm{NA}}e \tag{2.3}$$

where n is the refractive index of the specimen, M is the combined lateral magnification of the objective and zoom lenses, and e is the smallest distance that can be resolved by the image detector (measured on the detector's face plate). The wave optical depth of field is determined by one quarter of the distance between the first two diffraction minima, above and below focus. The geometrical optical depth is a result of the "circle of confusion." For example, a bright-field microscope using a 40 × /0.95NA objective lens and a CCD camera with 6.45 μm square pixels would have the field depth in water 1.0 μm at wavelength 546 nm. As it was shown by Inoué [10], the thickness of optical section (depth of field) of a conventional DIC microscope equipped with the same objective lens could be as little as 0.25 μm.

The contrast in DIC is produced by the optical path difference in a small in-focus volume where two interfering beams are spatially separated. Here, the beams travel through the different areas of the specimen under investigation. The out-of-focus object introduces practically the same phase disturbance in both the beams because the beams go through almost the same area of the specimen. Therefore, the out-of-focus disturbance is suppressed by optical subtraction. The optical section depth becomes thinner if the shear amount is smaller, and the objective and condenser NAs are larger. The narrow optical sectioning DIC phenomenon is similar to removing an out-of-focus haze in the structured illumination microscopy (SIM) [9]. The SIM employs a single-spatial-frequency grid pattern, which is projected onto the object under investigation. Raw images are taken at three spatial positions of the grid. The out-of-focus picture of the object does not depend on the pattern position. As a result, the out-of-focus haze in SIM is subtracted computationally.

Application of computation subtraction in the DIC would be expected to improve its sectioning capability even further. The computation subtraction of images with different biases is employed in various techniques, such as polarization modulation DIC (PM-DIC) [11,12], differential detection DIC (D-DIC) with polarizing beamsplitter [13], phase-shifting DIC (PS-DIC) [14−16], retardation modulation DIC (RM-DIC) [17−19], and orientation-independent DIC (OI-DIC) [6,20,21]. In particular, the PM-DIC removes a background contribution that is insensitive to defocus [12]. It is shown theoretically and confirmed experimentally that an RM-DIC microscope has stronger optical sectioning than a conventional DIC microscope, and the optical section depth is thinner if a Nomarski prism with smaller shear amount is used [19]. Our experiments with the OI-DIC microscope using 100 × /1.3NA oil immersion objective lens demonstrated the optical section depth about 0.1 μm. The corresponding field depth of a bright-field microscope would be 0.5 μm.

2.2 Measuring Shear Angle of DIC Prism

Shear amount (distance) is the critical parameter of a DIC microscope that determines its contrast, sensitivity, resolution, and optical section depth. Another issue with DIC microscopy is that, to derive quantitative information, one must know the amount of image shear. Generally, however, microscope manufacturers do not make that information available. As a result, one must measure this parameter. Munster et al. [22] determined the lateral shift by measuring the distance between the center of the bright spot and the center of the dark spot in an image of a submicroscopic transparent latex sphere with bias set at $\pi/2$. Mehta and Sheppard [23] measured shear by studying intensity distribution in the back focal plane of the microscope objective lens. Müller et al. [24] used a combination of fluorescence correlation spectroscopy and dynamic light scattering to determine shear. Duncan et al. [25] described a measurement setup with a standard optical wedge.

The technique described later for determining shear distance is simpler, faster, and more accurate than just mentioned. We measure a shear angle and then compute the shear amount by employing formula (2.1), as it is explained in the end of this section.

In order to find the shear angle of a DIC prism, we do not need to know how the passing beam is transformed inside the prism. A DIC prism splits an incident monochromatic plane wave into two orthogonally polarized plane waves with wavefronts of slightly different direction. Figure 2.2 illustrates splitting the incident linearly polarized beam into two separate output beams with shear angle ε. Here, the shear plane is parallel to the X-axis. As one can see in Figure 2.2, the shear angle ε (in radians) is equal to the derivative of the optical path difference (bias) Γ with respect to the coordinate x:

$$\varepsilon = \frac{\mathrm{d}\Gamma}{\mathrm{d}x} \tag{2.4}$$

The optical path difference Γ is connected with retardance δ, written in degrees, and wavelength λ in the simple way:

$$\Gamma = \frac{\delta}{360^\circ}\lambda \tag{2.5}$$

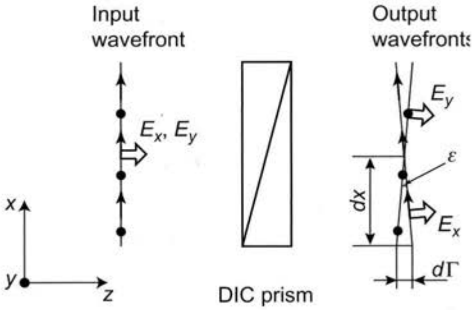

Figure 2.2
Splitting the incident beam with two orthogonal polarizations E_x and E_y by DIC prism into two separate output beams with shear angle ε.

Thus, the shear angle could be found by measuring a derivative of the retardance with respect to the coordinate along the shear direction:

$$\varepsilon = \frac{\lambda}{360^\circ}\frac{\mathrm{d}\delta}{\mathrm{d}x} \tag{2.6}$$

Retardance can be determined by a number of techniques. In particular, we employed the Senarmont compensator [26]. A schematic of the used setup is shown in Figure 2.3. A laser radiates the collimated narrow beam with horizontal linear polarization. Here, angle 0° corresponds to the horizontal direction (the X-axis). Then, the first quarter-wave plate QWP1, with fast axis oriented at 45°, transforms the linear beam polarization into the circular polarization. Polarizer, the second quarter-wave plate QWP2 and analyzer are mounted into rotatable holders with angular scale each. The DIC prism under investigation is placed on a linear stage with a Vernier micrometer. The stage allows movement of the prism in the horizontal direction. The minimum intensity of the passed laser beam was visually determined by observing the laser spot brightness on a screen.

The measuring procedure of retardance derivative consists of the following steps. Before placing the DIC prism under investigation in the setup, the prism is positioned between the crossed polarizers. The shear plane is perpendicular to the observed color fringes or/and the black fringe. The shear plane orientation is noted.

Next, the second quarter-wave plate, QWP2, is removed from the setup, cross polarizer and analyzer, and the DIC prism is positioned in the optical path. By rotating simultaneously

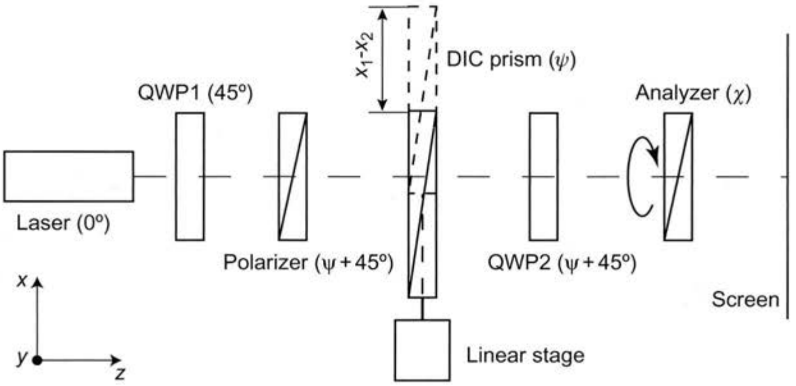

Figure 2.3

Setup for measuring shear angle of DIC prism by employing the Senarmont compensator. Laser with horizontally linearly polarized beam; QWP1: first quarter-wave plate at 45° azimuth; polarizer at $\psi + 45^\circ$ azimuth; DIC prism under investigation with shear plane azimuth at angle ψ; linear stage for shifting DIC prism in the horizontal direction; QWP2: second quarter-wave plate at $\psi + 45^\circ$ azimuth; rotatable analyzer at χ azimuth.

the polarizer and the analyzer from 0° to 180°, we achieve two extinctions of the laser spot on the screen. These extinctions differ by 90°. One extinction occurs when the polarizer transmission axis is parallel to the shear plane of the DIC prism. In this case, the polarizer angular scale points the shear plane orientation ψ. The other extinction corresponds to direction, which is perpendicular to the shear plane.

Next, the DIC prism is removed, and crossed polarizer and analyzer are rotated by 45°. If the orientation of the polarizer is $\psi + 45^\circ$, orientation of the analyzer is $\psi - 45^\circ$. The analyzer orientation is noted: $\chi_0 = \psi - 45^\circ$.

The second quarter-wave plate, QWP2, is then placed into the optical path. The fast axis of the quarter-wave plate must be parallel to the polarizer transmission axis. The laser spot on the screen extinguishes if the fast axis is precisely aligned.

Finally, the DIC prism under investigation is placed in the measuring setup. The laser spot becomes bright. Rotating the analyzer allows to extinguish the spot on the screen. The DIC prism retardance δ in a point of the laser beam incidence is determined by the simple formula:

$$\delta = 2(\chi - \chi_0) \tag{2.7}$$

where χ is the orientation angle of the analyzer.

Using a linear stage, the DIC prism is moved in the horizontal direction and retardances δ_1 and δ_2 are measured at two points x_1 and x_2. The retardance derivative along with the shear direction X could be found by the following formula:

$$\frac{\mathrm{d}\delta}{\mathrm{d}x} = \frac{\delta_1 - \delta_2}{(x_1 - x_2)\cos\psi} = \frac{2(\chi_1 - \chi_2)}{(x_1 - x_2)\cos\psi} \tag{2.8}$$

Then, we compute the shear angle (in radians):

$$\varepsilon = \frac{\lambda}{180^\circ}\frac{(\chi_1 - \chi_2)}{(x_1 - x_2)\cos\psi} \tag{2.9}$$

Instead of finding retardance values in two points only, we can measure dependence of the analyzer angle χ on the laser beam position x and use its derivative in formula (2.9):

$$\varepsilon = \frac{\lambda}{180^\circ}\frac{1}{\cos\psi}\frac{\mathrm{d}\chi(x)}{\mathrm{d}x} \tag{2.10}$$

In the described setup, we utilized generic green and red laser pointers. Wavelength of the green laser pointer was 532 nm and the red laser pointer was 641 nm. The achromatic quarter-wave plates were made by Bolder Vision Optik (Boulder, CO, USA, http://www.boldervision.com). Regular grade polarizers for the visible spectral range and the employed

Table 2.1: Measured Shear Angles, Computed Shear Distances, and Ratios of Shear Distance to Airy Disk Radius for Various Combinations of Olympus DIC Prisms and Objective Lenses at Wavelength 532 nm

DIC Prism Type	Shear Angle, ε	Shear Distance, d in μm (Ratio d/r_{Airy})						
		UplanFl 10×/0.30	UplanFl 20×/0.50	UplanSApo 30×/1.05 Sil	UplanFl 40×/0.75	UplanSApo 60×/ 1.20 W	UplanSApo 60×/1.30 Sil	UplanFl 100×/1.30 Oil
U-DICTHR	40 μrad	0.72 (0.67)	0.36 (0.55)	0.24 (0.78)	0.18 (0.42)	0.12 (0.44)	0.12 (0.48)	0.072 (0.29)
U-DICT	74 μrad	1.32 (1.23)	0.67 (1.03)	0.44 (1.44)	0.33 (0.77)	0.22 (0.82)	0.22 (0.89)	0.13 (0.53)
U-DICTHC	143 μrad	2.57 (2.38)	1.29 (1.98)	0.86 (2.78)	0.64 (1.49)	0.43 (1.59)	0.43 (1.72)	0.25 (1.03)

mechanical components were purchased from Thorlabs (Newton, NJ, USA, http://www.thorlabs.com).

Table 2.1 summarizes representative results of the shear angle measurements of various DIC prisms currently manufactured by Olympus (Tokyo, Japan, http://www.olympus.com). The high-resolution DIC prism U-DICTHR has the smallest shear angle. The prism enables observations with high resolution but with less glare even for thick specimens used in developmental and genetic research, such as finely structured diatoms, embryos, zebrafish and *Caenorhabditis elegans.* The general-use prism U-DICT with the intermediate shear angle is suitable for observing a wide range of general specimens, such as tissue. The high-contrast DIC prism U-DICTHC has the largest shear angle. Using this prism, high contrast can be obtained even in high-magnification observations of thin specimens, such as culture cells.

Table 2.1 shows also the corresponding computed shear distance d in the object plane and ratio of the shear distance to the Airy disk radius d/r_{Airy}. For the calculation, standardized reference focal lengths of the tube lenses L_t are used for infinity-focused objective lens, which are adopted by several microscope manufacturers.

$$d = \varepsilon \frac{L_t}{M} \tag{2.11}$$

In Eq. (2.11), M is the objective lens magnification. In particular, the reference focal length L_t is 180 mm for Olympus, 164.5 mm for Zeiss, and 200 mm for Nikon and Leica microscopes [9].

The radius of Airy disk r_{Airy} is determined by the following equation [9]:

$$r_{\text{Airy}} = 0.61 \frac{\lambda}{\text{NA}} \tag{2.12}$$

where NA is the objective lens numerical aperture.

The above data are shown for the green light ($\lambda = 532$ nm). The shear angle was about 4% less for the red light ($\lambda = 641$ nm).

We have measured parameters of the Olympus DIC prism U-DICTH, which was manufactured in previous years. Its shear angle is the same as the prism U-DICTHR. Mehta and Sheppard [23] found the angular shear of 74 μrad for the U-DICTS prism at wavelength 550 nm. This shear corresponds exactly to our observations for the U-DICT prism. Our other results indicate that shear angles of Nikon 60xI and Zeiss PA63x/1.40III DIC sliders are 76 and 71 μrad, respectively.

2.3 Bias Optimization

In polarization microscopy, the Bräce-Köhler compensator, an azimuthally rotatable birefringent plate with bias retardance up to $\lambda/10$, allows investigation of a specimen with small birefringence more precisely than the Senarmont compensator, which has a retardance of $\lambda/4$ [7,26]. For example, Swann and Mitchison [27], using the $\lambda/20$ Bräce-Köhler compensator, could detect a 0.028 nm retardation. In order to achieve high sensitivity with the LC-PolScope (a commercially available polarization microscope), we apply alternate bias retardance $\lambda/30$ [28,29]. The measured noise level using the five-frame algorithm was 0.036 nm. The bias $\lambda/5$, which was used for studying a sample with large retardance, produces much higher noise.

In conventional DIC microscopy, the situation is similar. Near extinction, the image field becomes dark gray and yields very high sensitivity, bringing out image regions with minute phase differences due to, for example, extremely shallow depressions or elevations or from isolated subresolution filaments. Use of bias less than 90° is advantageous in video-enhanced-DIC (VE-DIC) microscopy [30,31]. Holzwarth [12] studied a photon noise versus bias in PM-DIC microscopy. He showed theoretically and confirmed experimentally that the signal-to-noise ratio peaks when the bias equals the sample optical path difference.

The benefit of the optimized bias can be proved mathematically by using the following example. Let us consider a simplified sample with a binary gradient magnitude distribution such that half of the sample has a gradient magnitude of $+\gamma$ and the other half has a phase difference of $-\gamma$ (see Eq. (2.2)). The shear and gradient directions of the sample are parallel ($\theta = 0°$). We also take into account the depolarized light by using an extinction ratio $\xi = (I_c/\tilde{I})$.

We expect the best results to be achieved when the DIC images have the highest contrast C:

$$C = \frac{I_{\max} - I_{\min}}{I_{\max} + I_{\min}} \tag{2.13}$$

where $I_{\max}$ and $I_{\min}$ are the maximal and minimal intensities in the image.

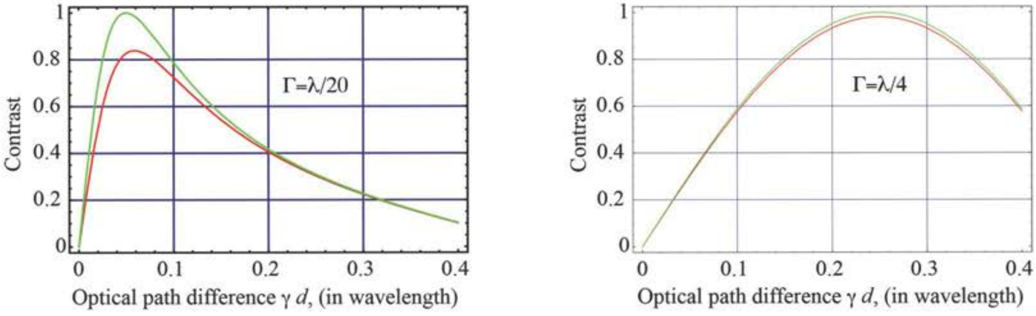

a)

b)

Figure 2.4

Contrast as a function of the sample optical path difference at biases 1/20th the wavelength (A) and quarter wavelength (B). The green color illustrates a case without depolarization (infinity extinction) and the red one corresponds to extinction 100. (For interpretation of the references to color in this figure legend, the reader is referred to the web version of this book.)

The maximal and minimal intensities can be determined using Eq. (2.2). For the specimen under consideration, the contrast of the DIC image is the following:

$$C = \frac{\sin((2\pi/\lambda)\Gamma)\sin((2\pi/\lambda)\gamma d)}{1 - \cos((2\pi/\lambda)\Gamma)\cos((2\pi/\lambda)\gamma d) + (2/\xi)} \tag{2.14}$$

Derivative $\partial C/\partial \Gamma$ of this equation is the next:

$$\frac{\partial C}{\partial \Gamma} = \sin\left(\frac{2\pi}{\lambda}\gamma d\right)\frac{(1 + (2/\xi))\cos((2\pi/\lambda)\Gamma) - \cos((2\pi/\lambda)\gamma d)}{1 - \cos((2\pi/\lambda)\Gamma)\cos((2\pi/\lambda)\gamma d) + (2/\xi)} \tag{2.15}$$

The derivative is zero at $\Gamma \approx \gamma d$. Thus, the best optical contrast is achieved when bias equals optical path difference in the sample. This result agrees with data obtained by Salmon and Tran [31]. They found that for the edges of organelles and cells, the optical path difference corresponds to about λ/10th the wavelength or greater but for microtubules and tiny organelles in cell, optical path difference is very small, less than 1/100th the wavelength of green light. Salmon and Tran recommend using about 1/15th−1/20th the wavelength bias for observation of microtubules in order to have sufficient light at the camera. A similar result was found by Schnapp [32].

Contrast curves computed with formula (2.14) at different biases and extinctions are given in Figure 2.4. According to Figure 2.4, the contrast of microtubules and tiny organelles with a phase difference λ/100 equals 0.38 at bias λ/20 and infinity extinction, 0.27 at bias λ/20 and extinction 100, and 0.06 at bias λ/4 and both extinctions. The contrast at the small bias is greater than 6 times the contrast at the large bias. However, it is very important to have a high extinction in order to effectively use a small bias for studying tiny structures. The contrast of cell walls and organelle edges with a phase difference $\lambda/10$ is 0.79 at bias $\lambda/20$ and infinity extinction, 0.72 at bias $\lambda/20$ and extinction 100, and 0.59 at bias $\lambda/4$ and both extinctions.

In addition to reducing contrast, the low extinction decreases the dynamic range of measurement and can cause a diffraction anomaly in the Airy pattern. The lower extinction is a significant problem in microscopes equipped with high NA lenses. To reduce the beam depolarization, we can use a polarization rectifier [33,34].

Most current DIC microscopes employ one of the following methods of changing bias: (a) lateral shift of the DIC prism using a screw, (b) the Senarmont compensator, or (c) liquid crystal variable retarder. In principle, it is also possible to use other means for the bias adjustment. For example, one can employ the Babinet-Soleil compensator [26], the Ehringhaus compensator [26,35], the Berek compensator [26,36], or its analogue made of quartz [37], electro-optic, or piezo-optical modulators [38]. All of these methods could be readily calibrated for the quantitative bias variation.

The total optical path difference (bias) between two interfering beams is created by combination of two DIC prisms (see Figure 2.1). Each of the prisms introduces bias, which is not uniform and has a gradient. However, the prisms are oriented such that they mutually compensate the bias gradient. Thus, the total bias distribution becomes even across the objective back focal plane. The bias can be changed by a lateral shifting of one of the DIC prisms along the bias gradient direction. As it was shown in Section 2.1 (formula (2.4)), the unitless bias gradient equals the shear angle (in radians). The linear equation for the current bias $\Gamma(x)$ is written:

$$\Gamma(x) = \Gamma_0 + \varepsilon(x - x_0) \tag{2.16}$$

where x and x_0 are the current and initial positions of the prism and Γ_0 is the initial bias. The shear angle ε can be found in Table 2.1 or it can be measured, as described in the previous section.

Usually, the DIC prism is shifted by a translation screw. Then, the bias variation is determined using the pitch of a screw thread p and revolution number R in the following way:

$$\Gamma(R) = \Gamma_0 + \varepsilon pR \tag{2.17}$$

For example, the Olympus high-resolution DIC prism U-DICTHR has a translation screw with pitch of 2.5 mm. The screw allows a maximum of five rotations. According to Table 2.1, the prism shear angle is 40 μrad. Using Eq. (2.17), the bias variation $\Gamma = 100$ nm per 360° turn of the screw and the total range of the bias change $\Gamma_{\text{tot}} = 500$ nm is calculated. The General Olympus DIC prism U-DICT has 3 mm screw pitch and maximum

5 rotations. Consequently, the bias variation Γ is 225 nm per screw turn and the total bias range Γ_{tot} is 1125 nm.

As described in Section 2.1, the Senarmont technique produces bias, which is linearly proportional to the analyzer rotation. Using formulae (2.7) and (2.5) we can find dependence of the bias Γ on the analyzer orientation angle χ:

$$\Gamma = \frac{\chi}{180^\circ}\lambda \tag{2.18}$$

Rotation of the analyzer from -90° to 90° introduces bias from $-\lambda/2$ to $\lambda/2$. The total bias range equals to one wavelength. The high bias accuracy is one of the advantages of the Senarmont method. For example, measuring the analyzer orientation with precision 0.1° will give the bias accuracy of 0.3 nm at wavelength 550 nm.

The liquid crystal variable retarder creates a bias, which depends on the applied voltage. However, this dependence is not linear. Therefore, it is necessary to have a calibration curve. The thinner liquid crystal variable retarders are faster and provide the bias change less than one wavelength. The thicker liquid crystals could give the bias change about two wavelengths. But they are considerably slower and more sensitive to the ambient temperature variation.

In order to create a large bias, it is possible to insert in the optical path an additional full-wave plate, which is also called the unit retardation plate or red plate [26]. This birefringent plate is cut of such a thickness as to have a retardation of one wavelength of yellowish green (550 nm), thus giving the sensitive first-order red between crossed polars in white light. Slight changes in the optical path difference by addition or subtraction of path differences by the specimen over which the plate is placed are very noticeable, and accordingly the plate is called a sensitive tint plate [39]. The color variation can be used for estimation of optical path difference of the specimen.

Figure 2.5 shows DIC images of 7 μm diameter glass rod immersed in Fisher Permount mounting medium (Fisher Scientific, http://www.fishersci.com). The refractive indices of the glass rod and the Permount at wavelength 546 nm were 1.554 and 1.524, respectively. The pictures were taken in white light using an Olympus BX-61 upright microscope equipped with the high-resolution DIC prism U-DICTHR, silicon oil objective lens UplanSApo30×/1.05Sil, photo eyepiece PE2.5× (Olympus America, http://www.olympusamerica.com), and Hamamatsu 3CCD Cooled Digital Color Camera ORCA-3CCD (Hamamatsu Photonics, http://www.hamamatsu.com). The shear plane is oriented in the northwest direction.

All images were captured with same exposure time, 0.1 s. Figure 2.5A represents a case when the bias is zero. Figure 2.5B was taken with bias of 100 nm (one full rotation of the translation screw). As one can see, the right bottom side of the rod is black. This means that

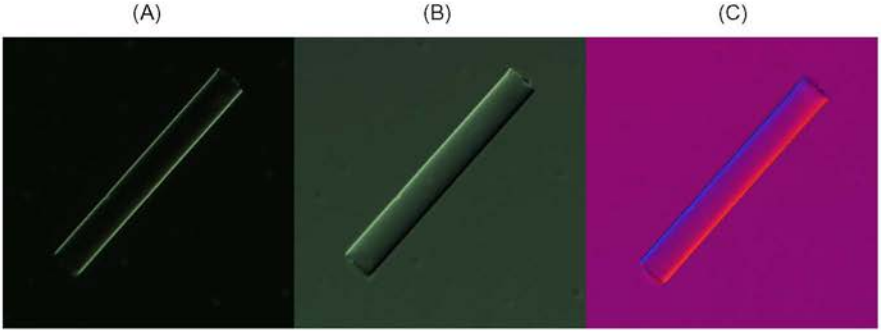

Figure 2.5
DIC images of 7 μm diameter glass rod captured in white light with zero bias (A), 100 nm bias (B), and 550 nm bias (C).

the optical path difference introduced by the rod side is subtracted by same amount of the bias (see formula (2.2)), and equals 100 nm. Figure 2.5C illustrates a case when bias is 550 nm. A full-wave plate U-TP530 was inserted in the optical path. Because the optical path difference is about one wavelength, the image shows Newton's interference colors. Then, the Michel-Levy chart is used to estimate the optical path difference [9,39]. The blue and orange colors of the rod sides correspond to 650 and 450 nm of optical path difference, respectively. After subtraction of the bias, the rod sides are shown to introduce about 100 nm of optical path difference. According to Table 2.1, the shear distance between the two interfering beams is 240 nm. Then, the optical path difference gradient of the rod side is 0.4 nm/nm. Hence, conventional DIC technique with calibrated bias can provide quantitative results.

2.4 A Quantitative OI-DIC Microscope with Fast Modulation of Bias and Shear Direction

OI-DIC technique records phase gradients within microscopic specimens quantitatively and independently of their orientation [6,20,21]. Unlike the other forms of phase and interference microscopes, this approach does not require a narrow illuminating cone. The new system is probably one of the few, if not the one and only, microscope system, which allows the generation of interference microscope images at truly high NAs.

A schematic of beam-shearing assembly with high speed switching shear direction and changing bias without any mechanical movement is shown in Figure 2.6 (center). The assembly consists of a linear polarizer P, first variable retarder (liquid crystal cell) LC1 with the principal axis orientated at 0°, a pair of DIC prisms (Nomarski or Wollaston) DIC1 and DIC2 with orthogonal shear directions, and second liquid crystal cell LC2 between the prisms. The second liquid crystal cell has the principal axis orientated at 45°.

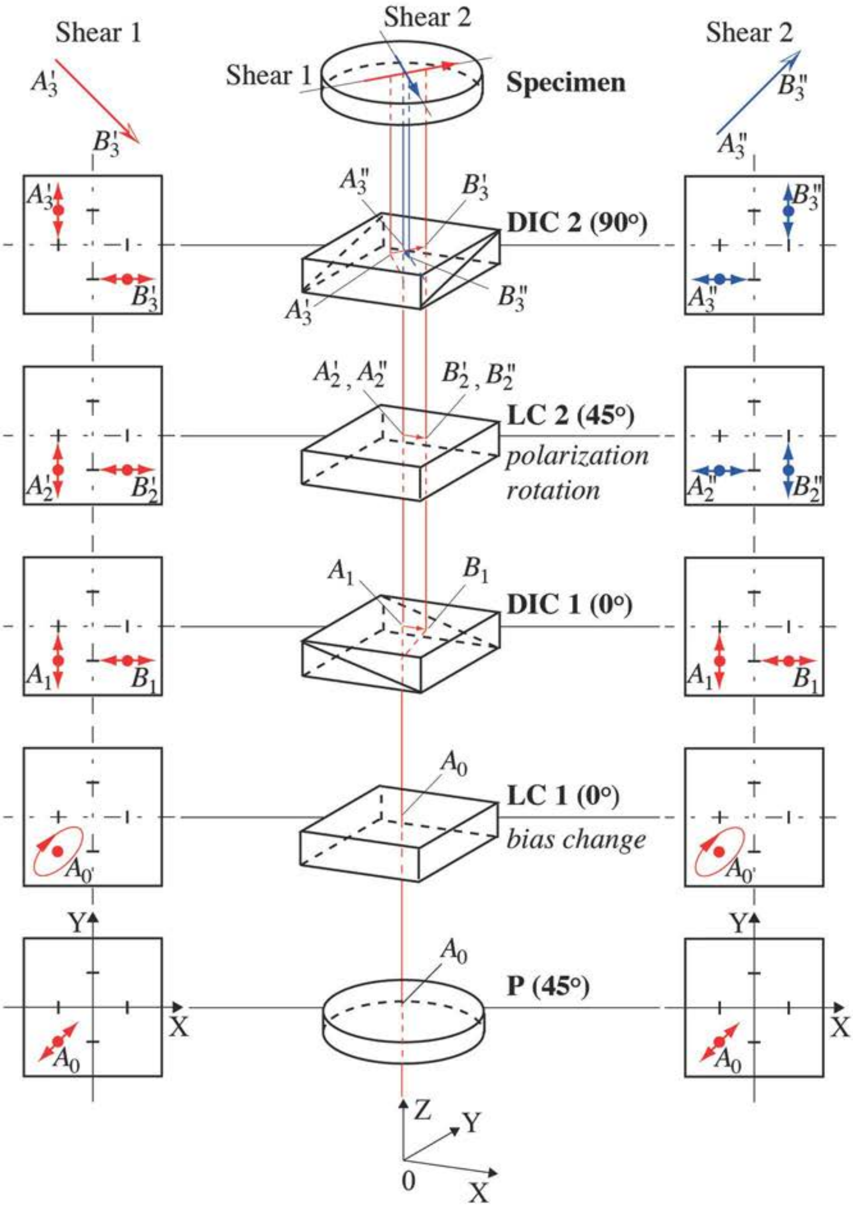

Figure 2.6

Schematic of switchable beam-shearing DIC assembly with liquid crystal variable retarders.

The shear direction of the first prism DIC1 is chosen as the initial X-direction to describe the orientation of the above-mentioned optical elements. The azimuth of the polarizer P is 45° in order to create equal intensities of polarization components that become spatially divided by the first prism. The first liquid crystal cell LC1 introduces bias Γ between the

X- and Y-polarization components, which depends on the applied voltage. The initial bias can be adjusted by sliding of the wedge component of one of the DIC prisms. In principle, the liquid crystal cell LC1 can be installed with the same orientation in any place in the assembly. The second liquid crystal cell LC2 switches the polarization by 90° when the plate retardation is a half wave ($\lambda/2$), and preserves the beam polarization if the plate retardance is 0 or full wave (λ).

The diagrams to the left and right in Figure 2.6 depict polarization transformations inside the assembly and the corresponding change of shear directions of the output beams. The left column illustrates a case when the beam polarizations between two prisms are preserved and the shear direction is 45° after the second prism DIC2. The right column describes a rotation of the output shear direction by 90° caused by switching the beam polarizations after the first prism DIC1.

Let us examine in more detail how the beam-shearing assembly works. For example, the initial ray A_0 falling on the first prism DIC1 has coordinates $(-1,-1)$. Here, the first number means a coordinate along the X-axis, and the second one is the coordinate along the Y-axis. The first DIC prism does not change the position of the ray with Y-polarization and deflects the ray with X-polarization, which creates a shear distance of two units between the two components. Thus, the first output ray A_1 has Y-polarization and coordinates $(-1,-1)$. If the shear value equals 2 units, then the X-polarized second ray has B_1 coordinates $(1,-1)$.

The second liquid crystal cell LC2 preserves the linear polarized states of the beams A_1 and B_1 or turns each of the states by 90° without altering the ray positions. In the first case (left column), the output rays A_2 and B_2 are polarized along the Y- and X-axis, respectively. In the second case (right column), the rays A_2 and B_2 are polarized along the X- and Y-axis, respectively.

The second DIC prism is oriented orthogonal to the direction of the first prism. So, the shear direction of the second prism lies along the Y-axis. The prism DIC2 does not change the position of a ray with X-polarization, but it deflects a ray with Y-polarization. The shear value for this second prism is also 2 units. First, we consider a case, which is shown on the left side of Figure 2.6, where the liquid crystal cell LC2 has retardance 0°, and therefore the ray polarizations are not changed. Then, ray A_2 with Y-polarization and coordinates $(-1,-1)$ passes the second prism with displacement by 2 units in the Y-direction, and the output ray A_3' has coordinates $(-1,1)$. Meanwhile, the coordinates of ray B_2 are not changed, and the coordinates for output ray B_3' are $(1,-1)$. As a result, in the first case, the dual beam that falls on the specimen has shear direction $-45°$.

For the second case, after the liquid crystal cell LC2 rotates the polarization by 90°, the ray A_2 is linearly polarized along the X-axis. Therefore, its coordinates are not changed by the second DIC prism, and the output ray A_3'' has coordinates (−1,−1). However, the second DIC prism moves the Y-polarized ray B_2 so that the second output ray B_3'' has coordinates (1,1). Hence, the output beam has a shear direction +45°.

In both the cases, the shears are the same, which is equal to the shear introduced by a single DIC prism multiplied by $\sqrt{2}$. However, the shear directions are mutually orthogonal. The median axis of two beams passes through point (0,0) in both the cases. Therefore, there is no misalignment between the images.

The intensity distribution in the image will be described by the transformed formula (2.2):

$$I_\mathrm{i}(x,y) = \tilde{I}\sin^2\left\{\frac{\pi}{\lambda}\left[\Gamma + \sqrt{2}d\gamma(x,y)\cos\left(\theta(x,y) - (-1)^i\frac{\pi}{4}\right)\right]\right\} + I_\mathrm{c}(x,y) \tag{2.19}$$

where $i = 1, 2$ corresponds to the first or second state of shear direction, −45° or +45°.

In order to find the two-dimensional distribution of magnitude and azimuth γ and θ, we capture two sets of raw DIC images at shear directions −45° and +45° with negative, zero, and biases: $-\Gamma$, 0, and $+\Gamma$ [6,20]. The following group of equations represents these six DIC images:

$$I_{ij}(x,y) = \tilde{I}\sin^2\left\{\frac{\pi}{\lambda}\left[j\Gamma + \sqrt{2}d\gamma(x,y)\cos\left(\theta(x,y) - (-1)^i\frac{\pi}{4}\right)\right]\right\} + I_\mathrm{c}(x,y) \tag{2.20}$$

where $j = -1, 0, 1$.

Initially two terms are computed ($i = 1, 2$):

$$A_i(x,y) = \frac{I_{i,1}(x,y) - I_{i,-1}(x,y)}{I_{i,1}(x,y) + I_{i,-1}(x,y) - 2I_{i,0}(x,y)}\tan\left(\frac{\pi\Gamma}{\lambda}\right) \tag{2.21}$$

Using Eq. (2.20), we can show that

$$\begin{aligned} A_1(x,y) &= \tan\left(\frac{2\sqrt{2}\pi}{\lambda}d\gamma(x,y)\cos\left(\theta(x,y) + \frac{\pi}{4}\right)\right) \\ A_2(x,y) &= \tan\left(\frac{2\sqrt{2}\pi}{\lambda}d\gamma(x,y)\sin\left(\theta(x,y) + \frac{\pi}{4}\right)\right) \end{aligned} \tag{2.22}$$

Using the obtained terms, we can calculate the quantitative two-dimensional distributions of the gradient magnitude and azimuth of optical paths in the specimen as:

$$\begin{aligned} \gamma(x,y) &= \frac{\lambda}{2\sqrt{2}\pi d}\sqrt{(\arctan A_1(x,y))^2 + (\arctan A_2(x,y))^2} \\ \theta(x,y) &= \arctan\left(\frac{\arctan A_2(x,y)}{\arctan A_1(x,y)}\right) - \frac{\pi}{4} \end{aligned} \tag{2.23}$$

The gradient magnitude represents the increment of the optical path difference, which is in nanometers, along the lateral coordinate, which is also in nanometers. Thus, the gradient magnitude is unitless. The shear amount d can be measured as it is described in Section 2.1 or found in Table 2.1.

Note that the algorithm considered earlier employs ratios between intensities of light that have interacted with the specimen. Therefore, it suppresses contributions of absorption by the specimen or from nonuniformity of illumination, which can otherwise deteriorate a DIC image.

Also, after computing the optical path gradient distribution, enhanced regular DIC images $I_{\mathrm{enh}}(x,y)$ can be restored with any shear direction σ, different bias Γ, and another shear amount d using the next formula:

$$I_{\mathrm{enh}}(x,y) = \sin^2\left\{\frac{\pi}{\lambda}[\Gamma + d\gamma(x,y)\cos(\theta(x,y) - \sigma)]\right\} \tag{2.24}$$

The enhanced image provides a calculated image for any desired shear direction and bias without the requirement to directly collect an image for that shear direction and bias. Moreover, the enhanced image will have less noise than a regular DIC image, and it suppresses deterioration of the image due to specimen absorption and illumination nonuniformity.

Optical path difference shows the dry mass distribution of a specimen and can be obtained by computing a line integral [6,40]. Also, other techniques for phase computation can be used, for instance, iterative computation [41], noniterative Fourier phase integration [15], or nonlinear optimization with hierarchical representation [42]. Biggs has developed an iterative deconvolution approach for computation of phase images, based on the same principles as deconvolution techniques normally used to remove out-of-focus haze [43–45].

In principle, a regular research grade microscope equipped with DIC optics can be modified for obtaining OI-DIC images. The setup was implemented on an upright microscope Olympus BX-61 (Olympus, Center Valley, PA, http://www.olympus.com). We built two custom beam-shearing DIC assemblies, one placed in the illumination path and the another in the imaging path (Figure 2.7). Using MATLAB (The MathWorks Inc., Natick, MA, http://www.mathworks.com/), we developed software for setup control and image processing.

Figure 2.8 shows an example of the phase OI-DIC image of a live crane fly spermatocyte during metaphase of meiosis I taken with an Olympus UPlanFl 100×/1.30 oil immersion objective lens and 546/30 nm interference filter. Image size is 68 μm × 68 μm. Here, the image brightness is linearly proportional to the phase (refractive index) distribution. The image acquisition and processing took about 1 s each. The three autosomal bivalent

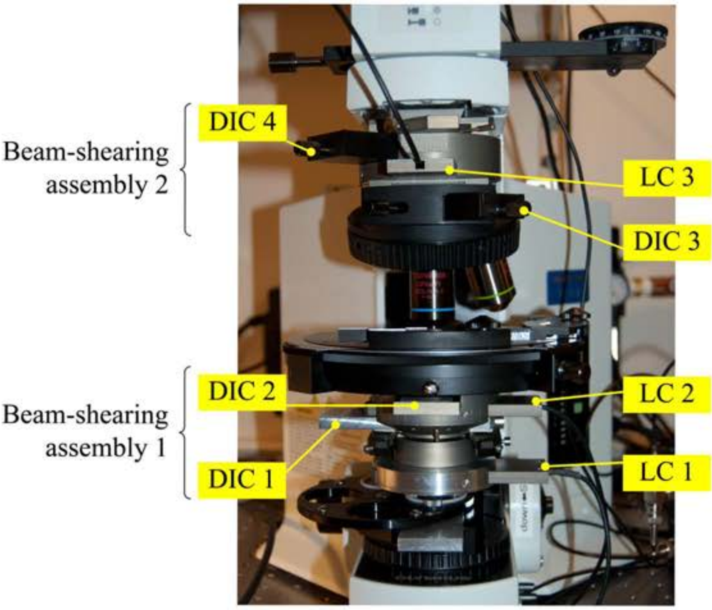

Figure 2.7
OI-DIC microscope setup with two switchable beam-shearing DIC assemblies. The first assembly consists of DIC prisms DIC1 and DIC2 and two liquid crystal variable retarders LC1 and LC2. The second beam-shearing DIC uses prisms DIC3 and DIC4 and liquid crystal variable retarders LC3.

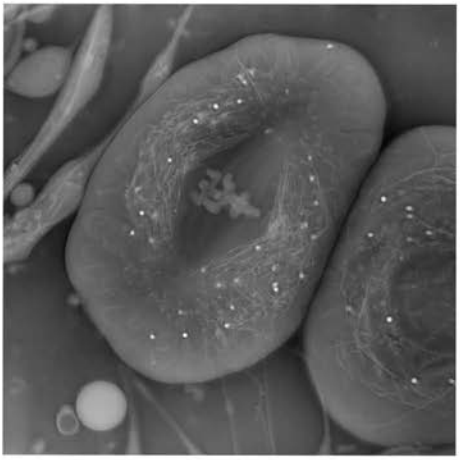

Figure 2.8
Phase OI-DIC image of live crane fly spermatocyte at metaphase of meiosis I.

chromosomes are in sharp focus at the spindle equator, along with one of the $X-Y$ sex univalents, which is located on the right. The tubular distribution of mitochondria surrounding the spindle is clearly evident. Both polar flagella in the lower centrosome are in focus, appearing as a letter "L" lying on its side. The experiment was done together with

Prof. James LaFountain (State University of New York at Buffalo, Buffalo, NY). The phase image was computed by Dr. David Biggs (KB Imaging Solutions, Waterford, NY) by employing the iterative deconvolution approach mentioned earlier.

The following are the comments made on this picture by MBL Distinguished Scientist Shinya Inoué:

> *The image is a real WOW! That is so striking; I have never seen such a view of a dividing cell, ever! Absolutely; have a huge blow up of this image for your poster at ASCB. The crane fly spermatocyte meiosis image is just mind blowing. You see the many thin-thread-shaped mitochondria surrounding the spindle, the chromosomes themselves and even the spindle fibers, all in striking 3-D. Also the scattered dyctiosomes show as prominent bright spots. But even more, the image shows some cytoplasmic structures that I had never seen in my life. Those must relate to Keith Porter's endoplasmic reticulum (membrane-related structures?) but in a different form. Their contrast is low but they definitely appear to be indented where astral rays would be expected. I don't think anyone has shown such structural differentiation of the cytoplasm until now, using any mode of microscopy whether in live or fixed and stained cells! In a nutshell this image shows the unusual capability of your orientation independent DIC system exceptionally well.*

2.5 Combination of OI-DIC and Orientation-Independent Polarization Imaging

DIC microscopy produces images of optical phase gradients in a transparent specimen, which is caused by variation of refractive index within thin optical section. Polarized light microscopy reveals structural or internal anisotropy due to form birefringence, intrinsic birefringence, stress birefringence, and other factors. An image in DIC microscope is determined by the optical phase distribution in the specimen, while an image in a polarized light microscope is produced by the polarization splitting of the optical phase caused by the specimen anisotropy. Thus, polarization microscopy data and DIC results are complementary. Both methods, however, have the same shortcomings: they require the proper orientation of a specimen in relation to the optical system in order to achieve high quality results, and the images are not quantitative. Hence, it would be beneficial to combine the OI-DIC microscope with an orientation-independent differential polarization (OI-Pol) system [45].

The differential OI-Pol microscope captures several images of the specimen with slightly different polarization settings of illumination or imaging beam [29,45–47]. Then, the images are subtracted one from another and further processed in order to obtain the quantitative picture of retardance and fast axis azimuth distribution.

The combined system is unique, providing complementary phase images of thin optical sections of the specimen that display a distribution of refractive index gradient and

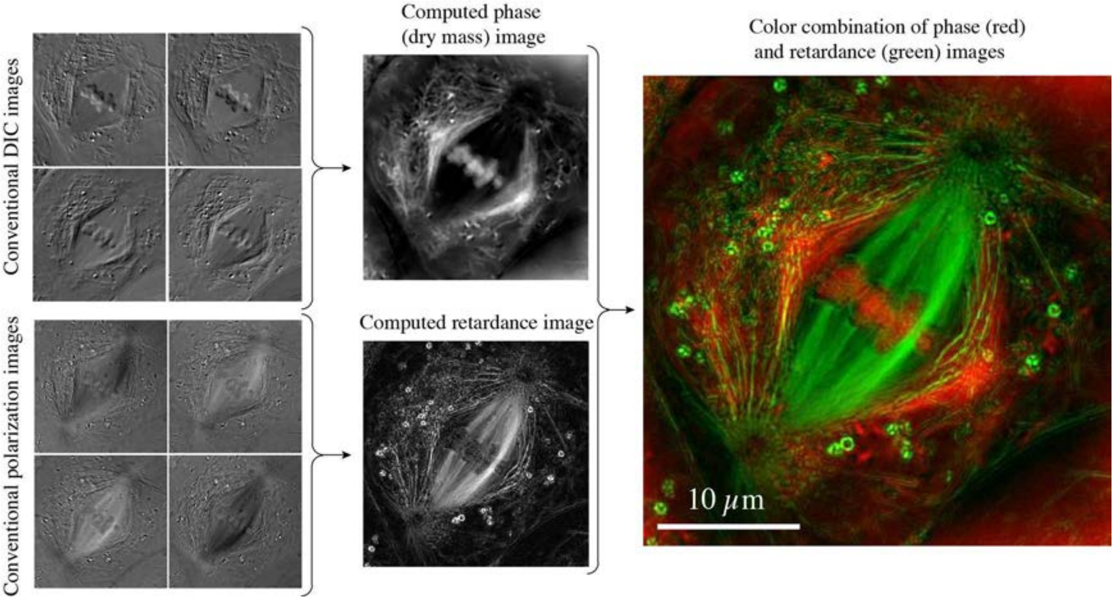

Figure 2.9

Metaphase of meiosis I in a crane fly spermatocyte. Color combination of phase (red) and retardance (green) images. (For interpretation of the references to color in this figure legend, the reader is referred to the web version of this book.)

distribution of birefringence due to structural or internal anisotropy of the cell structure. For instance, in a live dividing cell, the OI-DIC image clearly shows detailed shape of the chromosomes while the polarization image quantitatively depicts the distribution of the birefringent microtubules in the spindle, both without any need for staining or other modifications of the cell.

Figure 2.9 presents combined pseudo-color OI-DIC and OI-Pol image of spermatocytes from the crane fly, *Nephrotoma suturalis*, during metaphase of meiosis I. The experiment was done together with LaFountain. The phase image was computed by Biggs. The set-up was a Nikon Microphot-SA microscope equipped 60×/1.4NA oil immersion at wavelength 546 nm [45]. The changing of bias and rotating the shear direction during DIC image acquisition were done manually. Also, in order to switch between polarization and DIC imaging modes, the pair of liquid crystal waveplates was replaced with DIC prisms. At present, these mechanical manipulations take significant time relative to the temporal resolution of the test. A microscope which rapidly switches between the OI-DIC and the OI-Pol modes without any mechanical movement is theoretically possible and a prototype is in development.

The figure shows a group of 4 conventional DIC images (left top) and a group of 4 conventional polarization images (left bottom). These raw images were employed for computing phase (dry mass) and retardance images (middle top and bottom, accordingly). On the far right is a color combination of the phase (dry mass) and retardance modes, in which red and green colors correspond to dry mass distribution and retardance, respectively. Morphological structures, such as chromosomes, are especially prominent in the phase mode image. The birefringent spindle fibers (actually bundles of microtubules) exhibit much better contrast in the retardance mode. The combined picture provides clear evidence of our notion that the proposed technique can reveal architecture (morphology) of live cells without fluorescent labeling using 1.4NA optics.

2.6 Combination of OI-DIC and Fluorescence Imaging

In recent years, advances in fluorescent biosensors have made fluorescence imaging of living cells a key tool for cell biologists. However, quantitative data such as refractive indices and birefringences of whole specimens provide important information about protein concentration, density, and structural organization inside cells, but cannot be measured using fluorescence imaging. Although OI-DIC microscopy provides an extraordinary level of detail, the technique is more informative of cellular structures than of specific molecules. Fluorescence microscopy, on the other hand, provides detailed information on the distribution patterns of specific molecules and ions, but this information is often hard to interpret in the absence of additional structural information.

Combining fluorescence microscopy with OI-DIC imaging is an ideal technology that provides specificity of fluorescence and quantification of OI-DIC. For example, the type of organelles in a live specimen could be scored using fluorescence markers, and subsequent organelle development followed during a long time series using the OI-DIC with minimal phototoxicity.

Two schematics of the OI-DIC in combination with fluorescence microscopy were built: (1) simultaneous OI-DIC and fluorescence with two CCD cameras and (2) sequential OI-DIC and fluorescence with a switchable beamsplitter cube. Both approaches have been used successfully.

Figure 2.10 shows simultaneous images of chromosomes in a live *Spisula* oocyte treated with Hoechst 33342 (DNA-specific fluorescent dye) obtained by OI-DIC microscopy and wide field fluorescence microscopy. The micrographs were taken with a new Olympus 30×/1.05NA silicon oil objective lens UPLSAPO 30XS and photo eyepiece PE2.5×. The fluorescence image contains four selected square areas with chromosomes. These areas are enhanced in the computed quantitative gradient and phase images. The white level is 0.1 nm/nm in the enhanced areas and 0.3 nm/nm in other areas of the gradient picture. Brighter OI-DIC signal in the phase image indicates higher optical density, which corresponds to higher dry mass or concentration of the objects. The dry mass image of

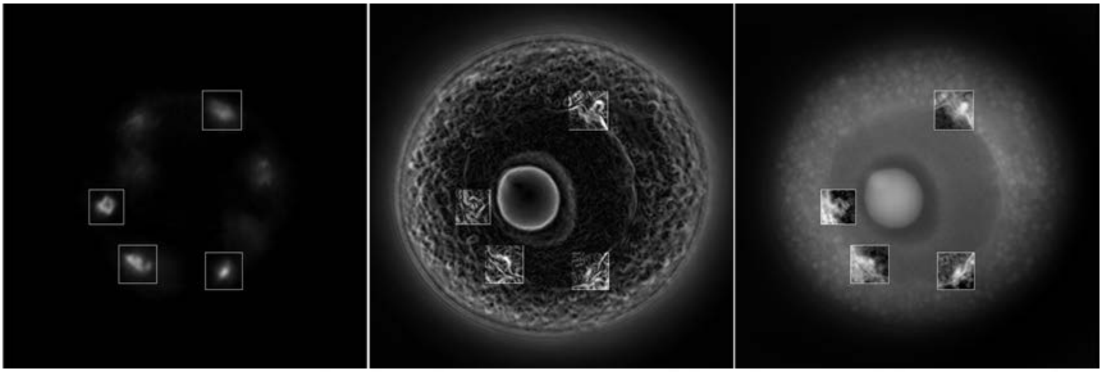
(A) (B) (C)

Figure 2.10
Simultaneous observation of live *Spisula* oocyte treated with DNA-specific fluorescent marker (Hoechst 33342) by (A) fluorescence and (B and C) OI-DIC microscopy techniques—(B) gradient and (C) phase (dry mass). Image size is 64 μm × 64 μm.

chromosomes is somewhat larger than the fluorescence image because it shows both proteins and DNA, while the fluorescence depicts stained DNA only.

This result indicates that OI-DIC can be used to visualize chromosomes in living cells and provides sufficient detail to recognize chromosomes by their dynamic individual three-dimensional shapes. OI-DIC imaging assessed the distribution of DNA in healthy living cells without using fluorescent DNA markers and irradiating with excess excitation light. Time-lapse imaging of DNA distribution during the mitotic phase of the cell cycle by this noninvasive methodology is an important tool. Moreover, as OI-DIC provides a two-dimensional distribution of the amount of DNA within an extremely thin optical section, OI-DIC enables reconstruction of the three-dimensional distribution of DNA in the nucleus.

Acknowledgment

This work was supported by NIH Grant Number R01-EB005710.

References

[1] F.H. Smith, Interference microscope, US Patent 2601175, (5 August 1947).
[2] F.H. Smith, Microscopic interferometry, Research (London) 8 (1955) 385.
[3] A.A. Lebedeff, Polarization interferometer and its applications, Rev. Opt. 9 (1930) 385.
[4] G. Nomarski, Interferential polarizing device for study of phase object, US Patent 2924142 (14 May 1952).
[5] R.D. Allen, G.B. David, G. Nomarski, The Zeiss–Nomarski differential equipment for transmitted light microscopy, Zeitschrift für Wissenschaftliche Mikroscopie und Mickroskopische Technik 69(4) (1969) 193.

[6] M. Shribak, S. Inoué, Orientation-independent differential interference contrast microscopy, Appl. Opt. 45 (2006) 460.
[7] M. Pluta, Advanced Light Microscopy. Vol. 2: Specialized Methods, Elsevier Science Publishing Co., Inc., New York, NY, 1989.
[8] S. Inoué, K.R. Spring, Video Microscopy: The Fundamentals, second ed., Plenum Press, New York, NY, 1989.
[9] R. Oldenbourg, M. Shribak, Microscopes, in: M. Bass (Ed.), Handbook of Optics, third ed., volume I: Geometrical and Physical Optics, Polarized Light, Components and Instruments, McGraw-Hill Professional, New York, NY, 2009 (chapter 28).
[10] S. Inoué, Ultrathin optical sectioning and dynamic volume investigation with conventional light microscopy, in: J. Stevens, L. Mills, J. Trogadis (Eds.), Three-Dimensional Confocal Microscopy: Volume Investigation of Biological Systems, Academic Press, San Diego, CA, 1994, pp. 397−419.
[11] G.M. Holzwarth, S.C. Webb, D.J. Kubinski, N.S. Allen, Improving DIC microcopy with polarization modulation, J. Microsc. 188(Pt 3) (1997) 249.
[12] G.M. Holzwarth, D.B. Hill, E.B. McLaughlin, Polarization-modulated differential-interference contrast microscopy with a variable retarder, Appl. Opt. 39 (2000) 6288.
[13] H. Ooki, Y. Iwasaki, J. Iwasaki, Differential interference contrast microscope with differential detection for optimizing image contrast, Appl. Opt. 35 (1996) 2230.
[14] P. Hariharan, M. Roy, Achromatic phase-shifting for two-wavelength phase-stepping interferometry, Opt. Commun. 126 (1996) 220.
[15] M.R. Arnison, K.G. Larkin, C.J.R. Sheppard, N.I. Smith, C.J. Cogswell, Linear phase imaging using differential interference contrast microscopy, J. Microsc. 214(Pt 1) (2004) 7.
[16] S.V. King, A.R. Libertun, C. Preza, C.J. Cogswell, Calibration of a phase-shifting DIC microscope for quantitative phase imaging, Proc. SPIE 6443 (2007) 64430M.
[17] H. Ishiwata, M. Itoh, T. Yatagai, A new method of three-dimensional measurement by differential interference contrast microscope, Opt. Commun. 260 (2006) 117.
[18] H. Ishiwata, M. Itoh, T. Yatagai, A new analysis for extending the measurement range of the retardation-modulated differential interference contrast (RM-DIC) microscope, Opt. Commun. 281 (2008) 1412.
[19] A. Noguchi, H. Ishiwata, M. Itoh, T. Yatagai, Optical sectioning in differential interference contrast microscopy, Opt. Commun. 282 (2009) 3223.
[20] M. Shribak, Orientation-independent differential interference contrast microscopy technique and device, US Patent 7233434, (17 December 2003).
[21] M. Shribak, Orientation-independent differential interference contrast microscopy technique and device, US Patent 7564618 (17 December 2003).
[22] E.B. van Munster, L.J. van Vliet, J.A. Aten, Reconstruction of optical path length distributions from images obtained by a wide-field differential interference contrast microscope, J. Microsc. 188 (1997) 149.
[23] S.B. Mehta, C.J.R. Sheppard, Sample-less calibration of the differential interference contrast microscope, Appl. Opt. 49 (2010) 2954.
[24] C.B. Müller, K. Weiß, W. Richtering, A. Loman, J. Enderlein, Calibrating differential interference contrast microscopy with dual-focus fluorescence correlation spectroscopy, Opt. Express 16 (2008) 4322.
[25] D.D. Duncan, D.G. Fischer, A. Dayton, S.A. Prahl, Quantitative Carré differential interference contrast microscopy to assess phase and amplitude, J. Opt. Soc. Am. A 28 (2011) 1297.
[26] N.H. Hartshorne, A. Stuart, Crystal and the polarizing microscope, fourth ed., Edward Arnold, London, 1970.
[27] M.M. Swann, J.M. Mitchison, Refinements in polarized light microscopy, J. Exp. Biol. 27 (1950) 226.
[28] M. Shribak, R. Oldenbourg, Sensitive measurements of two-dimensional birefringence distributions using near-circularly polarized beam, in Polarization Analysis, Measurement, and Remote Sensing V, D.H. Goldstein and D.B. Chenault (Eds.), Proc. SPIE, 4819 (2002) 56.
[29] M. Shribak, R. Oldenbourg, Technique for fast and sensitive measurements of two-dimensional birefringence distribution, Appl. Opt. 42 (2003) 3009.
[30] E.D. Salmon, VE-DIC light microscopy and the discovery of kinesin, Trends Cell Biol. 5 (1995) 154.

[31] E.D. Salmon, P. Tran, High resolution video-enhanced differential-interference contrast (VE-DIC) light microscopy, Methods Cell Biol. 56 (1998) 153.

[32] B.J. Schnapp, View single microtubules by video light microscopy, Methods Enzymol. 134 (1986) 561.

[33] M. Shribak, S. Inoué, R. Oldenbourg, Rectifiers for suppressing depolarization caused by differential transmission and phase shift in high NA lenses, in Polarization Analysis, Measurement, and Remote Sensing IV, D.H. Goldstein and D.B. Chenault (Eds.), Proc. SPIE 4481 (2001) 163.

[34] M. Shribak, S. Inoué, R. Oldenbourg, Polarization aberrations caused by differential transmission and phase shift in high NA lenses: theory, measurement and rectification, Opt. Eng. 41 (2002) 943.

[35] D.A. Holmes, Wave optics theory of rotary compensators, J. Opt. Soc. Am. A 54 (1964) 1340.

[36] F. Rinne, M. Berek, Anleitung zu Optischen Untersuclhungen mit dem Polarizationsmikroskop, Schweizerbart'sche Verlagsbuchhandlung, Stuttgart, Germany, 1953.

[37] M. Shribak, Use of gyrotropic birefringent plate as quarter-wave plate, Sov. J. Opt. Technol. 53 (1986) 443.

[38] A. Yariv, P. Yeh, Optical Waves in Crystals: Propagation and Control of Laser Radiation, John Wiley & Sons, New York, NY, 1984.

[39] F.E. Wright, The Methods of Petrographic-Microscopic Research, Carnegie Inst., Washington, DC, 1911.

[40] B. Heise, A. Sonnleitner, E.P. Klement, DIC image reconstruction on large cell scans, Microsc. Res. Tech. 66 (2005) 312.

[41] C. Preza, Rotational-diversity phase estimation from differential-interference-contrast microscopy images, J. Opt. Soc. Am. A 17 (2000) 415.

[42] F. Kagalwala, T Kanade, Reconstructing specimens using DIC microscope images, IEEE Trans. Syst. Man Cybern. Part B Cybern. 33 (2003) 728.

[43] T.J. Holmes, S. Bhattacharyya, J.A. Cooper, D. Hanzel, V. Krishnamurthi, W. Lin, et al., Light microscopic images reconstructed by maximum likelihood deconvolution, in: J.B. Pawley (Ed.), Handbook of Biological Confocal Microscopy, Plenum Press, New York, NY, 1995, pp. 389–402.

[44] D. Biggs, M. Andrews, Acceleration of iterative image restoration algorithms, Appl. Opt. 36 (1997) 1766–1775.

[45] M. Shribak, J. LaFountain, D. Biggs, S. Inoué, Orientation-independent differential interference contrast microscopy and its combination with an orientation-independent polarization system, J. Biomed. Opt. 13 (2008) 014011.

[46] R. Oldenbourg, G. Mei, New polarized light microscope with precision universal compensator, J. Microsc. 180 (1995) 140.

[47] M. Shribak, Complete polarization state generator with one variable retarder and its application for fast and sensitive measuring of two-dimensional birefringence distribution, J. Opt. Soc. Am. A 28 (2011) 410.